Performance of a high fill factor, indirect detection prototype flat-panel imager for mammography

Youcef El-Mohri,[a] Larry E. Antonuk, Qihua Zhao, Yi Wang, Yixin Li, Hong Du, and Amit Sawant
Department of Radiation Oncology, University of Michigan Medical Center, Ann Arbor, Michigan 48109

(Received 17 May 2006; revised 4 October 2006; accepted for publication 8 November 2006; published 26 December 2006)

Empirical and theoretical investigations of the performance of a small-area, high-spatial-resolution, active matrix flat-panel imager, operated under mammographic conditions, is reported. The imager is based on an indirect detection array incorporating a continuous photodiode design, as opposed to the discrete photodiode design employed in conventional flat-panel imagers. Continuous photodiodes offer the prospect of higher fill factors, particularly for arrays with pixel pitches below ~100 μm. The array has a pixel-to-pixel pitch of 75 μm and a pixel format of 512×512, resulting in an active area of $\sim 3.8 \times 3.8$ cm^2. The array was coupled to two commercially available, structured CsI:Tl scintillators of ~150 μm thickness: one optimized for high light output (FOS-HL) and the other for high spatial resolution (FOS-HR), resulting in a pair of imager configurations. Measurements of sensitivity, modulation transfer function (MTF), noise power spectra (NPS), and detective quantum efficiency (DQE) were performed with a 26 kVp mammography beam at exposures ranging from ~0.5 to ~19 mR. MTF results from both CsI:Tl scintillators show that the array demonstrates good spatial resolution, indicating effective isolation between adjacent pixels. The effect of additive noise of the system on DQE was observed to be significantly higher for the FOS-HR scintillator compared to the FOS-HL scintillator due to lower sensitivity of the former. For the FOS-HL scintillator, DQE performance was generally high at high exposures, limited by the x-ray quantum efficiency, Swank factor and the MTF of the scintillators. For both scintillators, the DQE performance degrades at lower exposures due to the relatively large contribution of additive noise. Theoretical calculations based on a cascaded systems model were found to be in general agreement with the empirically determined NPS and DQE values. Finally, such calculations were used to predict potential DQE performance for hypothetical 50 μm pixel pitch imagers, employing similar continuous photodiode design and realistic inputs derived from the empirical measurements.
[DOI: 10.1118/1.2403967]

Key words: digital mammography, active matrix flat-panel imager, detective quantum efficiency, continuous photodiode, cascaded systems model

I. INTRODUCTION

Following several decades of research and development, digital mammography has become a reality with a variety of commercial imaging systems being introduced as replacements for screen-film systems. For example, one type of imager employs a slot-scanning detection process in which the x-ray image is acquired by means of a collimated, narrow detector that is mechanically scanned in one direction. One such imager uses four tiled charge coupled devices (CCDs) and a CsI:Tl scintillator to convert x rays into optical photons.[1] Other examples are photon counting systems that employ either a thick crystalline silicon detector[2] or a gas detector.[3] Yet other systems employ area detection such as complementary metal-oxide-semiconductor (CMOS) arrays[4] and active matrix, flat-panel imagers (AMFPIs).[5–8] While digital mammography systems generally offer imaging performance comparable to screen-film systems,[9] they also offer a number of advantages including wide dynamic range, high detection efficiency, contrast enhancement and, in some cases, the possibility for advanced imaging techniques such as computer aided diagnosis,[10,11] dual-energy imaging,[12] tomosynthesis[13] and computed tomography (CT).[14,15]

An AMFPI system is based upon an array consisting of a two-dimensional matrix of imaging pixels. Each pixel contains a thin-film transistor (TFT) used to control the storage and readout of the imaging signal. AMFPIs employ one of two detection methods: "indirect" detection in which a scintillating screen is used to convert incident x rays into light photons which are subsequently converted into electrons by photodiodes; and "direct" detection in which a photoconductive material is used to directly convert incident x rays into electrons. For indirect detection, a system based on a 100 μm pixel pitch, flat-panel array with discrete (i.e., isolated) amorphous silicon (*a*-Si:H) photodiodes and a structured CsI:Tl scintillator, is commercially available. The performance of this imager, in terms of the detective quantum efficiency (DQE), has been characterized for various mammographic exposures.[6] More recently, performance enhancements achieved through improvements in the CsI:Tl converter and additive noise have been reported.[16] (Additive

noise refers to the electronic noise of the imaging system when it is operated in the absence of radiation.) For direct detection, large-area commercial systems employing *a*-Se photoconductors at pixel pitches of 70 and 85 μm have been introduced.[7,8] Results from these direct and indirect detection flat-panel imagers indicate that, over the spatial frequency range provided by the imagers, their DQE performance is comparable or superior to that of mammographic screen-film systems. At low exposures, however, DQE performance degrades as a result of the limited signal size compared to the relatively large additive electronic noise contribution.[17,18]

The performance of mammographic digital imagers at low exposures is gaining more importance with the advent of novel imaging techniques such as tomosynthesis[13] and computed tomography[14,15] which require multiple images per exam to acquire volumetric information. The success of these techniques is predicated upon the acquisition of a series of high quality, low exposure images while maintaining an overall patient dose equivalent to that for a single conventional projection image. Since AMFPIs are based on full area detection, they are well suited to such novel imaging techniques. Therefore, research efforts are underway to improve their performance at low exposures, not only for mammography, but also for other applications such as fluoroscopy.[19] In the case of mammography, the challenge is compounded by the desire to achieve high spatial resolution to assist in the visualization of microcalcifications, potentially requiring a pixel pitch as low as 50 μm. Achieving such a small pixel pitch constitutes a challenge for present-day AMFPI technology since large reductions in signal size and the corresponding signal-to-noise-ratio are to be expected. For the indirect detection approach involving discrete photodiodes, an additional challenge impeding the development of such high resolution AMFPIs is the fact that the fraction of the pixel that is optically sensitive, referred to as the fill factor, decreases dramatically for designs with pitches less than $\sim$100 μm. The sole indirect detection mammographic AMFPI system currently available has a 100 μm pixel pitch and a reported fill factor of 75%.[20] For the direct detection approach, no limitations on fill factor have thus far been observed, as demonstrated by near-unity fill factor reported on the commercial system employing an 85 μm pitch array.[8] For indirect detection using conventional design rules for array fabrication, a fill factor of only $\sim$4% is to be expected at 50 μm pitch, as indicated in Fig. 1. [These design rules are based on the assumption that, in a pixel, the light sensing element (the photodiode), the switching element (the thin-film transistor) and the address lines (gate and data lines) do not overlap. Therefore, any reduction in pixel pitch is generally achieved by means of reducing the photodiode area.] Even with aggressive design rules such as those used to enhance the fill factor of recent prototype indirect detection arrays,[21] a fill factor of only $\sim$58% can be expected at 50 μm pitch.[22] To overcome this limitation, our group, in collaboration with scientists at the Palo Alto Research Center, has been exploring the development of novel, continuous photodiode structures to supplant the discrete photodiode design.[17,23,24] Using this approach, near-unity fill factors have been achieved for sub-100 μm pitches.[23]

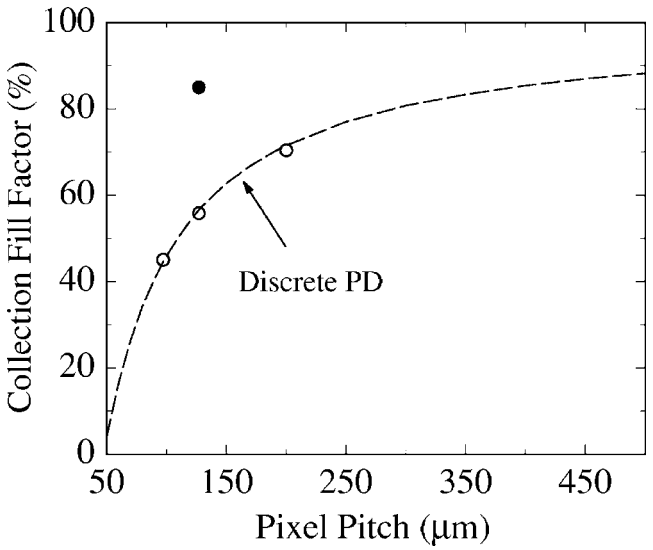

FIG. 1. Signal collection fill factor plotted as a function of pixel-to-pixel pitch for conventional arrays employing discrete photodiode designs. The dashed line shows calculations based on array design rules used in contemporary, commercial arrays, while the open circles correspond to three indirect detection flat-panel array designs developed with discrete photodiodes (Refs. 34, 57, and 58). The solid circle corresponds to a recent, prototype, discrete photodiode design employing considerably more aggressive design rules (Ref. 21).

In this paper, performance evaluations of signal, modulation transfer function (MTF), noise power spectra (NPS) and detective quantum efficiency (DQE) from an indirect detection prototype imager employing a continuous photodiode design are reported. These empirical results are compared with predictions from a model based on cascaded systems theory.[19,25,26] The model is also used to examine the potential DQE performance of 50 μm pitch hypothetical imagers employing this novel design, as well as other signal-enhancing designs pursued by our group. These initial studies are part of a comprehensive program of research to develop mammographic AMFPI technologies that offer significantly improved performance.

II. METHODS AND MATERIALS

A. Flat-panel imager

1. HOFFA array

The flat-panel imager examined in this study incorporates an array with a format of 512×512 pixels and a pitch of 75 μm, giving an active area of 3.84×3.84 cm^2. Design specifications of this array, which will be referred to as HOFFA (high optical fill factor array),[23] are summarized in Table I. This array incorporates a continuous photodiode design as opposed to the discrete design presently employed in all commercial indirect detection AMFPIs. This new design involves the deposition of *p-i-n a*-Si:H photodiode layers having a bottom (*n*) "patterned" layer and continuous *i* and *p* upper layers, followed by a top indium tin oxide (ITO) layer, as illustrated in Fig. 2. The *n*-doped bottom layer overlays a

TABLE I. Design specifications of the flat-panel array (HOFFA) used in these studies. The geometric photodiode area and fill factor correspond to the area of the collection electrode.

Pixel format (data × gate)	512 × 512
Pixel pitch	75 μm
Array dimension	3.84 × 3.84 cm^2
Data line capacitance	~15 pF
TFT dimensions ($L \times W$)	10 × 15 μm^2
Geometric photodiode area	~4036 μm^2
Geometric fill factor	~72%

metal collection electrode used to collect charge created in the *i* layer. Patterning of the *n*-layer creates charge collection "islands," thereby ensuring a high degree of electrical isolation between adjacent pixels.[27] In this design, the area of the collection electrode is maximized by forming a "mushroom" structure similar to that used in direct detection AMFPIs (Ref. 28) in order to help maximize charge collection. This configuration results in a gap of ~10 μm between adjacent pixels and a geometric fill factor, defined as the area of the collection electrode relative to the pixel area, of ~72%. However, by virtue of the continuous upper layers of the photodiode design, most of the charge created in the gap is collected resulting in an effective optical fill factor that is close to unity.[29] It should be noted, however, that the observed near-unity fill factor is a result of maximizing the geometric fill factor (i.e., the area of the collection electrode). A previous study has shown that reduction in the geometric fill factor through an increase in the gap between pixels results in a reduction of the optical fill factor.[30]

The use of continuous upper layers in the photodiode design could potentially promote charge sharing between adjacent pixels, and thus contribute to spatial resolution degradation. However, previous studies have shown that these effects are generally small and only become non-negligible at high incident illuminations corresponding to signal levels close to pixel saturation.[27] Specifically, if a pixel is illuminated to the point of saturation, while keeping the adjacent pixel nonilluminated, charge sharing (i.e., cross talk) of ~5% is observed as a result of lateral conduction between the collection electrodes of the pixels.[27] For example, slight spatial resolution degradation may be encountered during breast imaging in the vicinity of the skin surface where exposure to the detector is high. An additional problem posed by the continuous upper photodiode layers is the additional capacitance formed between the top metal electrode (ITO) and the underlying address lines. In particular, this increases the data line capacitance, which in turn leads to higher additive electronic noise due to larger noise contributions from the readout preamplifiers.[18] To reduce this problem, the present HOFFA array incorporates a new type of passivation material to insulate the photodiode from the underlying data lines.[31] Compared to the passivation material incorporated in many modern arrays, which consists of ~1-μm-thick silicon oxinitride, SiON, with a dielectric constant of ~5, this new passivation material involves a 3-μm-thick layer of a polymer-based resin (BCB, Dow Chemical), with a dielectric constant of

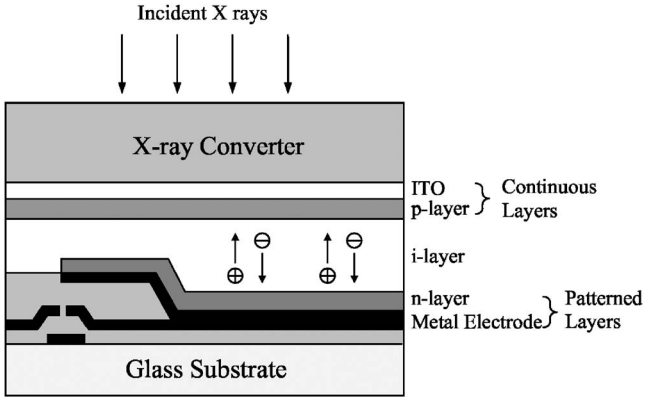

FIG. 2. Schematic illustration showing a cross-sectional view of an array employing a continuous photodiode structure.

2.6. Thus, BCB offers the possibility of constructing arrays with continuous photodiode structures with minimal increase in the data line capacitance. In the case of the present HOFFA array, the introduction of BCB insulator results in a data line capacitance per pixel of ~30 fF,[31] which corresponds to a total capacitance of ~15 pF.

For the conditions under which the array was operated for the current studies, the pixel dark current was low, ~3 fA—corresponding to ~0.6 pA/mm^2. This compares favorably with dark current values exhibited by commercial indirect and direct detection AMFPI devices that are on the order of 0.5–1 pA/mm^2.[5] However, the dark current was also observed to decrease linearly with time, with the amount of drift varying pixel by pixel and continuing for hours following the application of bias. (The origin of the observed drift is suspected to be at least partially due to the temporal decay of dark current caused by the depletion of electrons from the intrinsic *a*-Si:H layer of the photodiode.[32] Such effects should be reduced with improvement to the quality of the photodiode material, as has been found for discrete photodiode array designs.) While temporally constant pixel-to-pixel nonuniformities are normally removed by means of image processing in the form of gain and offset corrections,[33] temporally varying nonuniformities are more difficult to properly account for, especially at low exposures where the magnitude of x-ray signal can be on the order of the magnitude of dark signal drift. In the present study, a careful pixel-by-pixel drift correction, based on mapping the dark signal behavior with time, was successfully applied to the data prior to application of a standard gain and offset correction, as detailed in Sec. II B 1. Finally, measurements of charge trapping (using techniques described in Ref. 34) yielded a value of ~26%—higher than levels of 5%–15% obtained from high quality discrete photodiode indirect detection arrays.[5]

2. X-ray converters

The HOFFA array was coupled to two different CsI:Tl scintillators allowing two imaging configurations to be studied. The scintillators, whose physical properties are tailored to mammographic imaging, were used to convert incident x rays into light photons. Each scintillator consisted of

~150-μm-thick, structured (i.e., needle-like) CsI:Tl grown on a 3-mm-thick fiber optic plate (FOS, Hamamatsu) comprising ~3–6-μm-diam bundled fibers: one optimized for high light output (FOS-HL) and the other for high resolution (FOS-HR).[35] The CsI:Tl scintillators, with dimensions of 5 $\times$5 cm^2, were positioned in close contact with the array using the fiber optic faceplate, which serves as a light guide. Optical coupling between the array and the fiber optic plate was maintained by the latter exerting its own weight on the array without the use of an additional coupling medium. Since both surfaces are rigid, any surface nonuniformities could result in unintended air gaps. In this present case, however, it was determined that if any air gaps existed, they would be less than ~20 μm.

3. Electronic acquisition system

The measurements were performed using an electronic acquisition system specifically designed to allow detailed studies of the performance of imaging arrays such as the HOFFA array.[36] The system incorporates full-custom, low noise, 32-channel preamplifier-multiplexor chips.[37] When operated with the HOFFA array, the system has an additive noise performance, σ_{add}, in the range of ~1200 e (rms) to ~2200 e (rms). This range of noise values corresponds to frame times ranging from ~0.37 to ~2.27 s, corresponding to the various mammographic radiation exposures used in the present study. For all measurements, the gate line voltages used to render the pixel TFTs conducting and nonconducting were +10 and −8 V, respectively. The bias voltage applied across the continuous photodiode was set to ~−4 V.

B. Experimental methodology

All x-ray measurements were performed using a mammographic x-ray source (Senographe DMR, GE Medical Systems) at an energy of 26 kVp. A molybdenum (Mo) target was used with an intrinsic beam filtration of 30 μm Mo. The x-ray beam was further hardened by a compression paddle and a 5-cm-thick breast phantom[38] (tissue-equivalent BR12, Nuclear Associates), which approximates 50% glandular tissue and 50% adipose tissue. The surface of the imager was positioned at a source-to-detector distance of 65 cm and the phantom was placed ~40 cm above the imager. The mAs control of the unit was adjusted to provide the desired radiation exposure to the imager resulting in exposure times ranging from ~0.05 to ~2 s. The magnitude of the exposure to the imager surface was determined using a calibrated ion chamber (Keithley 96035B) and a dosimeter (Keithley 35050A). Values of exposure ranged from ~0.5 to ~19 mR. The imager was operated in radiographic mode with array readout synchronized to the radiation beam by means of a trigger pulse generated by the electronic acquisition system.[34] The width of the trigger pulse is adjusted so as to ensure that the radiation is delivered before array readout, resulting in an exposure level-dependent frame time.

1. Dark signal drift correction

The HOFFA array exhibited dark signal drift that resulted in a time-dependent pixel-to-pixel nonuniformity. The magnitude of the drift is such that the application of gain and offset corrections to remove this nonuniformity is less effective as time elapses between the acquisition of the correction constants and the actual image, especially for small x-ray signals obtained at the lowest exposures. In this case, drift artifacts appear in the image as a type of structure noise. In order to correct for drift, all x-ray measurements were preceded by a series of dark signal measurements. Due to the fact that the drift was observed to be linear within the span of time required for the measurements (several minutes), it was possible to apply a linear fit to dark signal data in order to detrend the effect of drift pixel-by-pixel from both dark and x-ray measurements. Within the time span over which the flood data were acquired, the amount of dark signal drift was observed to vary by approximately 5–10 analog-to-digital convertor (ADC) channels. Given that, at the lowest exposures (~0.5 mR), x-ray signal using the FOS-HR configuration was only ~13 ADC channels, the amount of dark signal drift would have a deleterious effect on x-ray signal determination if no correction were applied. In addition, since the amount of drift was not uniform from pixel to pixel, NPS measurements could be seriously affected at low exposures in the absence of drift correction. For example, after drift correction, the NPS results are improved by approximately a factor of 3 in the case of the FOS-HR configuration at 0.5 mR.

2. Modulation transfer function

Spatial resolution of the two imaging configurations was characterized by determination of the MTF, which was obtained from the Fourier transform of the line spread function (LSF). Measurements of the LSF were performed at a mammographic energy of 26 kVp with a Mo/Mo target/filter combination and no additional filtration. Additional filtration was found to have negligible effect on the MTF. For each imaging configuration, LSF data were obtained using the angled-slit technique.[39] The slit consists of a circular, 3-cm-diameter Tantalum disk, 1.5 mm thick with a central opening of ~0.01$\times$7 mm^2 (Slit Camera, Nuclear Associates). For each measurement, five radiographic images of the slit were obtained with the slit tilted at a small angle (~2°) with respect to either the gate line or the data line direction, corresponding to the measurement of resolution along the scanning direction or the orthogonal direction, respectively. For each image, gain and offset corrections were applied in order to compensate for nonuniformities in pixel-to-pixel response. For each measurement, the corrected images were averaged resulting in a single image from which the LSF was determined.

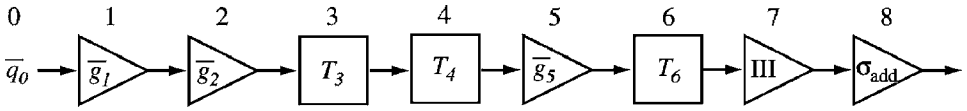

FIG. 3. Block diagram representing the various stages constituting the imaging chain in the cascaded systems analysis of the imaging configurations involving the HOFFA array. The number printed on top of each stage represents the order in the imaging chain. See Table II and the main text for details.

3. Noise power spectra and detective quantum efficiency

One-dimensional noise power spectra, NPS(u), were determined for each of the imaging configurations of the prototype imager. NPS(u) corresponds to a central slice through the origin of the two-dimensional noise power spectrum NPS(u,v), along one primary axis [NPS(u)=NPS(u,v)$|_{v=0}$]. This axis corresponds to the gate line direction. Earlier analyses with active matrix flat-panel imagers have indicated that one-dimensional NPS results, NPS(u), obtained along the gate line direction are consistent with those obtained along the orthogonal (data line) direction, NPS(v), except for the presence of one or more peaks due to correlated noise pickup from power supply and other electromagnetic sources.[26,40] The methodology used to measure NPS follows that described in previous publications.[26,41] For each imaging configuration and exposure, a total of 50 "flood-field" frames were acquired with x-ray irradiation and 50 "dark-field" frames were acquired in the absence of x-ray irradiation. (While the flood-field frames are used to determine the NPS associated with the corresponding exposure level, dark-field frames are used to determine dark NPS values which served as an input to a theoretical model of the system NPS [see Sec. II C].) Each frame was then cropped to a smaller, central region consisting of 320×320 pixels with minimum defects. After application of a drift correction, followed by gain and offset corrections (with the offset correction only applied in the case of the dark fields), a 3×3 median filter was applied to each frame in order to correct for faulty and nonfunctioning pixels, affecting less than 0.3% of the total number of pixels. After converting pixel signal values into electrons by means of an independently measured calibration factor for the preamplifiers (1 ADC=550 e^-), NPS were determined using the synthesized slit technique.[42–44] This technique involved the selection of independent, nonoverlapping blocks of pixels, each with dimensions of $L\times n$ (32×160) pixels, with the long dimension oriented along the gate line direction. Each data block was then summed along the L direction giving a 160 point realization. After subtraction of low-frequency background trends and the application of a Hanning window function, a Fourier transform was applied to each of the realizations. The results were then normalized[26] to yield an ensemble of 1100 power spectra, the average of which resulted in the measured NPS. For each imaging configuration and exposure, the measured NPS was used to determine DQE using the following equation:[6,45,46]

$$\mathrm{DQE}(u)=\frac{\bar{d}^2\mathrm{MTF}^2(u)}{\bar{q}_0\mathrm{NPS}(u)}, \tag{1}$$

where $\bar{d}$ is the mean signal in units of electrons derived from the NPS flood-field data, $\bar{q}_0$ is the incident x-ray fluence (x-ray photons per unit area), and MTF is the measured modulation transfer function.

C. Cascaded systems model

A theoretical model, based on the cascaded systems formalism,[25,46] was developed to reproduce the empirical results of signal, NPS, and DQE of the two imaging configurations of the HOFFA array as well as to predict the performance of hypothetical imaging configurations. In this model, the imaging system is divided into a series of stages where each stage represents a physical process. The signal and noise transfer properties of the imaging system are determined by the transfer properties of each stage.[47] Figure 3 shows a simplified diagram illustrating the various stages representing the imaging system used in this study while the parameters describing the system are shown in Table II. A detailed description of the various stages depicted in Fig. 3 can be found in Ref. 48 and is briefly summarized as follows. Stage 0 represents the incident x rays characterized by an incident fluence, $\bar{q}_0$ (x rays/unit area), Stage 1 represents the interaction of a fraction of the incident x rays with the scintillator with a quantum efficiency, $\bar{g}_1$. Stage 2 represents the generation and emission of optical photons by the interacting x rays in the scintillator with a quantum gain, $\bar{g}_2$. The optical photons undergo multiple scattering before exiting the scintillator resulting in a blurring mechanism characterized by a

TABLE II. Terms and symbols used in the cascaded systems model shown in Fig. 3.

Imaging System Parameters and Miscellaneous Symbols	
X	Exposure (mR)
$\bar{q}_0$	Mean x-ray fluence (x rays/mm^2)
$\bar{g}_i$	Gain of stage i
ϵ_{g_i}	Poisson excess associated with a gain stage i
I	Swank factor
T_i	MTF of stage i
S_i	Output noise (NPS) of stage i
S_{add}	Additive noise ($e^2\times\mathrm{mm}^2$)
σ_{add}	Additive noise (e[rms])
III	Sampling grid represented by a 2D comb function
(u,v)	Spatial frequency coordinates (mm^{-1})

MTF represented by T_3 (stage 3). After exiting the scintillator, photons may undergo further scattering between the exit surface of the scintillator and the HOFFA array, resulting in a blurring mechanism characterized by T_4. (Note that the representation of this process by a single blurring stage is equivalent to representation by parallel stages as in Ref. 48.) Stage 5 represents the coupling of the optical photons to the photodiode with a gain, $\bar{g}_5$, and stage 6 represents the integration of these photons by a square photodiode aperture of a side length, a_{pd}, characterized by an MTF T_6. Stage 7 represents sampling of the signal from the two-dimensional array of pixels with a pixel-to-pixel pitch of a_{pix} related to a_{pd} by the relation

$$a_{\mathrm{pd}}^2 = a_{\mathrm{pix}}^2 \times \text{fill factor}. \tag{2}$$

Since the fill factor of the present HOFFA array is close to unity, a_{pd} was assumed to be equal to a_{pix} in the calculations. Finally, stage 8 represents a readout of the imaging signal by the acquisition electronics characterized by an additive noise, S_{add}, where $S_{\mathrm{add}}=\sigma_{\mathrm{add}}^2 \times a_{\mathrm{pix}}^2$.

Using the cascaded systems formalism and the aforementioned stages of the imaging system, an expression for x-ray sensitivity per pixel was derived based on the product of the gains of the stages

$$\Gamma = \left(\frac{\bar{q}_0}{X}\right) a_{\mathrm{pd}}^2 \bar{g}_1 \bar{g}_2 \bar{g}_5 \quad (e/\mathrm{mR}). \tag{3}$$

In this expression, X represents the exposure (in units of mR) at the surface of the imager. The noise power spectra $S(u,\nu)$ can be expressed as follows:[48]

$$S(u,\nu) = a_{\mathrm{pd}}^4 \bar{q}_0 \bar{g}_1 \bar{g}_2 \bar{g}_5 [1 + \bar{g}_5(\bar{g}_2 + \epsilon_{g_2}) T_3^2(u,\nu) T_4^2(u,\nu)] \times T_6^2(u,\nu)^{**} III(u,\nu) + S_{\mathrm{add}}(u,\nu) \quad (e^2\ \mathrm{mm}^2). \tag{4}$$

In this expression, the process of sampling is represented by the convolution of the presampled NPS with the Fourier transform of the sampling grid, $III(u,\nu)$. The sampling grid may be written as

$$III(u,\nu) = \sum_{k,l=-\infty}^{\infty} \delta(u - k u_s, \nu - l \nu_s), \tag{5}$$

where u_s and ν_s correspond to sampling frequencies, given by the inverse of a_{pix}. In Eq. (4), S_{add}, an empirical input to the model, is the dark NPS, which corresponds to the additive noise. S_{add} was measured in the manner previously described in Sec. II B 3. For the calculation of DQE, the expression shown in Eq. (1) was used. In this expression, NPS is simply the calculated NPS, $S(u,\nu)$, MTF is the product of system MTF components (T_3, T_4, and T_6) and $\bar{d}$ is the product of sensitivity, Γ, and exposure, X, resulting in the following expression for DQE:

$$\mathrm{DQE}(u,\nu) = \frac{a_{\mathrm{pd}}^4 \bar{q}_0 [\bar{g}_1 \bar{g}_2 \bar{g}_5 T_3(u,\nu) T_4(u,\nu) T_6(u,\nu)]^2}{S(u,\nu)}. \tag{6}$$

In the determination of theoretical system performance in terms of sensitivity, NPS and DQE, the various parameters were either deduced from empirical data, obtained from the imager configurations, or obtained from published results. A summary of values of parameters used in the calculations are summarized in Table III. The detection efficiency of the converter ($\bar{g}_1$) was obtained from EGS4 Monte Carlo simulations based on the geometry and physics reported in Ref. [48]. In the simulations, a previously reported mammographic spectrum[49] based on a 26 kVp peak energy and Mo/Mo target filter combination was used. The spectrum was hardened by a BR12 phantom and a compression paddle, using the appropriate total mass attenuation data. In the calculations, the thickness of the BR12 phantom was slightly adjusted in comparison to the actual phantom so that the calculated half-value layer matches that obtained from measurements (0.63 mm). The phantom has an elemental composition and associated weight fraction [in percent], of H[9.6], C[70.3], N[1.9], O[17.0], Cl[0.2], and Ca[0.9], and a density of 0.98 g/cm^3. The compression paddle was simulated by 3 mm of Plexiglas with an elemental composition of H[8], C[60], and O[32], and a density of 1.19 g/cm^3. In the determination of x-ray fluence per unit exposure ($\bar{q}_0/X$), an appropriate normalization was performed to account for the polyenergetic nature of the spectrum.[50]

TABLE III. Summary of system parameters employed in the model shown in Fig. 3 and their associated values for a 26 kVp incident x-ray beam. The modeled x-ray beam corresponds to a Mo/Mo (target/filter) combination with an additional filtration of BR-12 breast phantom. The thickness of the phantom (6.5 cm) was chosen so that the modeled beam gives a half-value layer matching the corresponding measurement (0.63 mm). In the calculations, the additive electronic noise, σ_{add}, ranged from 1200 to 2200 e [rms], depending on the exposure, and the value of $\bar{g}_5$ was reduced by 26% in order to account for the signal loss due to the trapping of charge in the photodiode.

System parameters	FOS-HL configuration	FOS-HR configuration
$\bar{q}_0/X$ (x rays/mm^2/mR)	46 520	46 520
$\bar{g}_1$	0.83	0.83
$\bar{g}_2$	312	161
ϵ_{g_2}	5.26	2.22
I	0.98	0.98
$\bar{g}_5$	0.45	0.45

The scintillators were modeled using a cylindrical geometry with a 20 cm radius, and a thickness of 150 μm of CsI:Tl for FOS-HR and FOS-HL, with the assumption of 100% packing density. (Although the assumed packing density is larger than typical values of 75%, the combined values of thickness and density used in the model reflect the actual amount of CsI contained in the samples.) The modeled geometry consisted of a pencil beam of photons incident at the center of one end of the cylinder defining the scintillator and perpendicular to the surface. For the Monte Carlo histories generated in the simulations, x-ray interactions and the energy deposited in the scintillator were recorded by generating the absorbed energy distribution (AED). AED is defined as the distribution of x-ray energy absorbed following each x-ray interaction. The AED was calculated by tabulating the energy deposition over all histories using an energy bin size

of 0.5 keV. The gain $\bar{g}_1$ was obtained by dividing the number of x rays that interact in the scintillator by the total number of incident x rays. The quantum gain ($\bar{g}_2$) is defined as the mean number of optical quanta exiting the scintillator per interacting x-ray:

$$\bar{g}_2 = \gamma \frac{\bar{E}_{ab}}{\bar{E}_{opt}}, \tag{7}$$

where γ is the screen conversion efficiency,[51] defined as the efficiency of the scintillator in converting x-ray absorbed energy into optical photons. In this definition, γ includes both the intrinsic screen conversion efficiency and the probability of optical photons exiting the scintillator. $\bar{E}_{opt}$ is the mean energy of optical photons emitted by the scintillator (2.2 eV), determined from the emission spectrum of the scintillator,[35] and $\bar{E}_{ab}$ is the mean energy absorbed per interacting x ray, estimated from the calculated AED. The screen conversion efficiency (γ) was deduced from Eq. (7), with $\bar{g}_2$ obtained from Eq. (3) by fitting the sensitivity calculated from that expression to the corresponding measurements for each FOS scintillator. For FOS-HL, the deduced value of γ was 0.036 while for FOS-HR it was 0.019. These values of γ account for light attenuation in the 3-mm-thick fiber optic plate which is coupled to the scintillators. The mean optical transmission of such a plate has been estimated to be only ~60%.[35]

The term ϵ_{g_2} in Eq. (4) represents the Poisson excess in $\bar{g}_2$ and was obtained from the equation[25]

$$\epsilon_{g_2} = \bar{g}_2 \left(\frac{1}{I} - 1 \right) - 1, \tag{8}$$

where I is the Swank factor, which quantifies the noise associated with the x-ray to light conversion process and is mainly determined by two factors, the absorbed energy distribution (AED), and the optical pulse distribution (OPD):

$$I = I_{AED} I_{OPD}. \tag{9}$$

In this study, the Swank factor was assumed to be dominated by the absorbed energy distribution in the scintillators, resulting in a value of 0.98 for the 26 kVp x-ray spectrum used.[48]

The average optical coupling efficiency ($\bar{g}_5$) was determined from the integral of the product of the CsI:Tl scintillator emission spectrum[34] and the absorption spectrum of the *a*-Si:H photodiodes,[23] resulting in a value for $\bar{g}_5$ of 0.61 for both FOS-HL and FOS-HR screens. Since mammographic measurements are obtained radiographically, resulting in a signal loss due to charge trapping in the *a*-Si:H photodiodes, it was necessary to account for this loss in the model through a correction to $\bar{g}_5$. For the exposure conditions of the present study, and for the corresponding signal levels obtained with both FOS-HL and FOS-HR scintillators, charge trapping was empirically determined through independent measurements and found to be ~26%. The application of such a correction to $\bar{g}_5$ resulted in a final value of ~0.45.

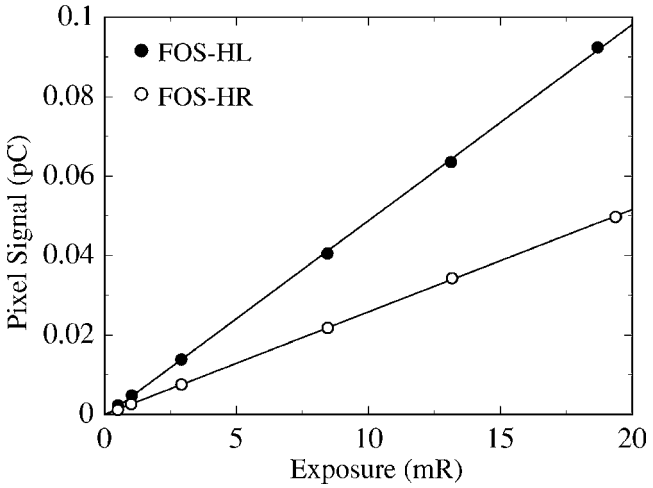

FIG. 4. Measured pixel signal as a function of exposure for imager configurations employing FOS-HL and FOS-HR scintillators.

The MTF of the entire system can be represented by the product of MTFs in the present model:

$$T_{sys}(u,v) = T_3(u,v) T_4(u,v) T_6(u,v), \tag{10}$$

where, for each scintillator, T_3 was obtained from published data,[35] and T_6 is a sinc function corresponding to the aperture of each square photodiode (the aperture is assumed to be equal to a_{pix} due to the near-unity fill factor of the HOFFA array). T_4 was deduced for each scintillator using Eq. (10) and the empirically determined system MTF.

III. RESULTS

A. X-ray sensitivity

X-ray response of the HOFFA array employing both FOS-HL and FOS-HR scintillators is shown in Fig. 4. The response is seen to be linear within the range of exposures used (~0.5 to ~19 mR), corresponding to up to ~4% of the pixel charge capacity. The FOS-HL scintillator is seen to provide about a factor of 2 more signal compared to the FOS-HR scintillator, consistent with the expectation that the latter has been optimized for high spatial resolution at the expense of light output. Linear fits to the data of Fig. 4 result in slope values corresponding to sensitivities of ~30 900 e/mR and ~16 200 e/mR for FOS-HL and FOS-HR scintillator, respectively.

B. Modulation transfer function (MTF)

Figures 5(a) and 5(b) show MTFs corresponding to resolution along the gate line direction for the imager configurations employing the FOS-HL and FOS-HR scintillators, respectively. For each configuration, measured (presampling) system MTF is shown along with the scintillator MTF (T_3)[35] as well as the sinc function corresponding to a 75 μm photodiode aperture (T_6). As expected, FOS-HR configuration exhibits higher measured system MTF values compared to the FOS-HL configuration by virtue of the higher resolution performance of the scintillator. The MTF values at the Ny-

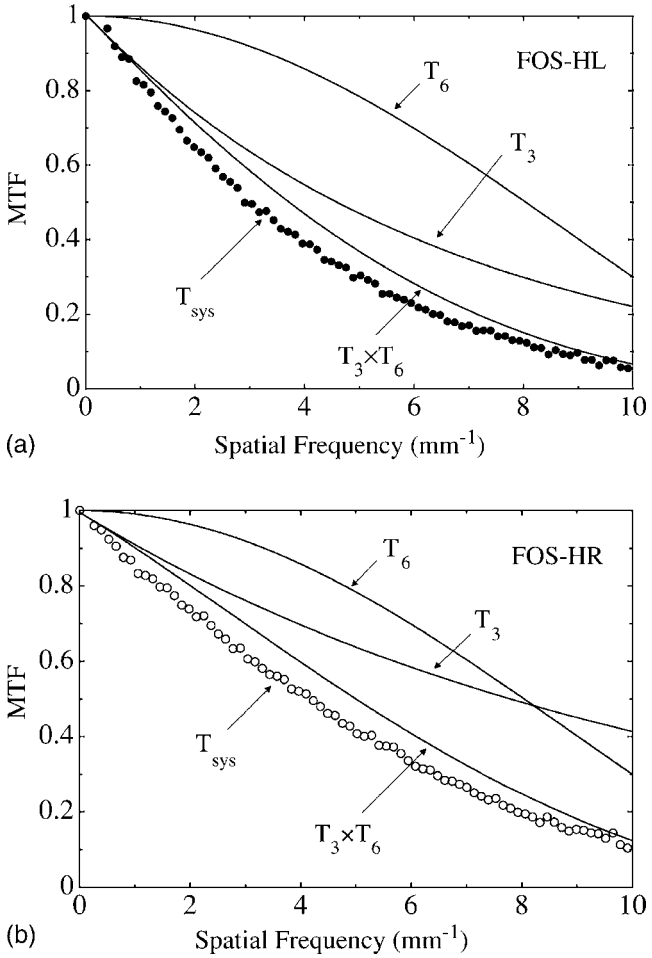

FIG. 5. Modulation transfer functions (MTFs) associated with (a) the FOS-HL imager configuration and (b) the FOS-HR imager configuration. For each configuration, the measured system MTF (T_{sys}), the MTF of the scintillator (T_3) and the sinc function corresponding to the 75 μm photodiode aperture (T_6), as well as the product of T_3 and T_6, are shown.

quist frequency of 6.66 mm^{-1} are ~0.18 and ~0.28 for FOS-HL and FOS-HR configurations, respectively. For both configurations, the product of the sinc function and the scintillator MTF results in a MTF that is slightly higher than the measured system MTF. The difference has been attributed to an additional MTF component (referred to T_4 in the cascaded model) due to nonideal optical coupling between the converter and the HOFFA array. In fact, additional blurring due to possible charge sharing between adjacent pixels of the array could also contribute to the observed difference. However, since this effect is short ranged and occurs from pixel to pixel through lateral conduction, it is most likely to affect the MTFs only at high spatial frequencies. Given that the measured system MTFs are systematically lower than the product of the sinc function and the scintillator MTFs over most of the frequency range, the difference is most likely to be dominated by the coupling effects (T_4) rather than blurring due to charge sharing. Finally, for each scintillator configuration, measurements of spatial resolution in the orthogonal direction corresponding to the direction of the data lines resulted in identical MTF values.

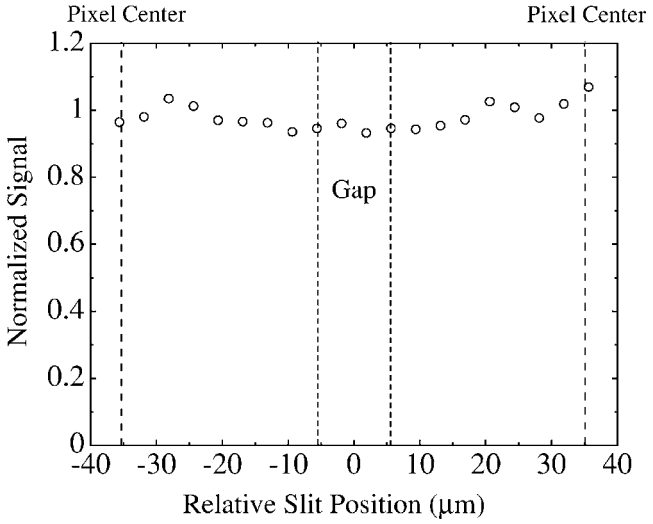

FIG. 6. Data illustrating the relative optical efficiency across the pixel surface of an array. The data were obtained from images of a ~10 μm-wide slit positioned at a small angle with respect to the data line direction for purposes of MTF measurements. Each point represents signal summed across a single row of pixels along a gate line—where data from many frames were averaged in order to minimize statistical fluctuations. The signal results have been normalized so that the average of the presented points is unity. The points are plotted as a function of the position of where the gate line crosses the slit, relative to the center of the gap between electrodes of neighboring pixels. The long dashed lines indicate the location of the centers of adjacent, neighboring pixels while the short dashed lines correspond to the location of the edges of electrodes for those pixels, defining the region of the gap.

In order to verify the near-unity fill factor of the HOFFA array, MTF slit images, that were used to determine MTFs of the imager configurations employing FOS-HL and FOS-HR scintillators, were further analyzed in a manner similar to that previously reported.[8,52] The result, plotted in Fig. 6 in terms of summed, normalized pixel signal versus position relative to the center of the ~10-μm-wide gap between electrodes of neighboring pixels, shows no apparent reduction of signal due to signal loss in this gap. This result is in line with an earlier finding that the HOFFA array exhibits a near-unity fill factor and supports the assumption of unity fill factor in the cascaded systems model.

C. Noise power spectra (NPS)

Figures 7(a) and 7(b) show NPS results corresponding to the HOFFA imager configurations employing the FOS-HL and FOS-HR scintillators, respectively. For each configuration, NPS is shown for six x-ray exposure levels, namely, ~0.5, ~1.0, ~2.9, ~8.5, ~13.2, and ~19 mR (more precisely, 18.7 mR for FOS-HL and 19.4 mR for FOS-HR). Except for the lowest exposures where the contribution of additive noise is relatively important, the NPS exhibit an approximately linear increase with increasing exposure, as expected. For the FOS-HL configuration, the absolute magnitude of the NPS is shown to be larger than that of the FOS-HR configuration due to the correspondingly higher sensitivity. However, for the FOS-HL configuration, the NPS is found to decrease significantly with increasing spatial frequency as compared to the FOS-HR configuration, in accor-

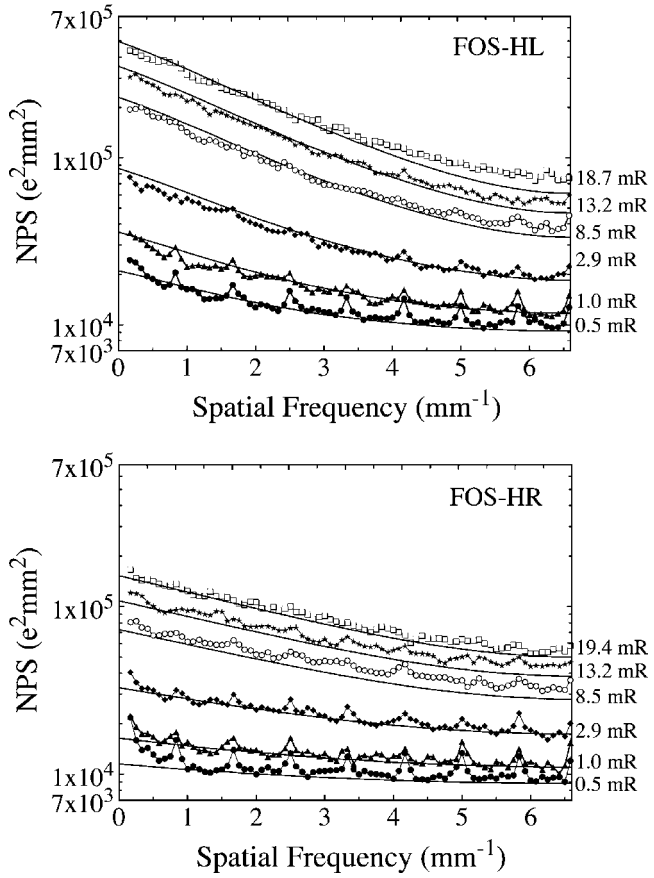

FIG. 7. Noise power spectra (NPS) associated with (a) the FOS-HL imager configuration and (b) the FOS-HR imager configuration. Measured (symbols) and calculated (lines) NPS are presented for a variety of exposure levels. For the calculations, contributions of the empirically determined, electronic additive noise, which ranged from ~1200 *e* [rms] to ~2200 *e* [rms], were included.

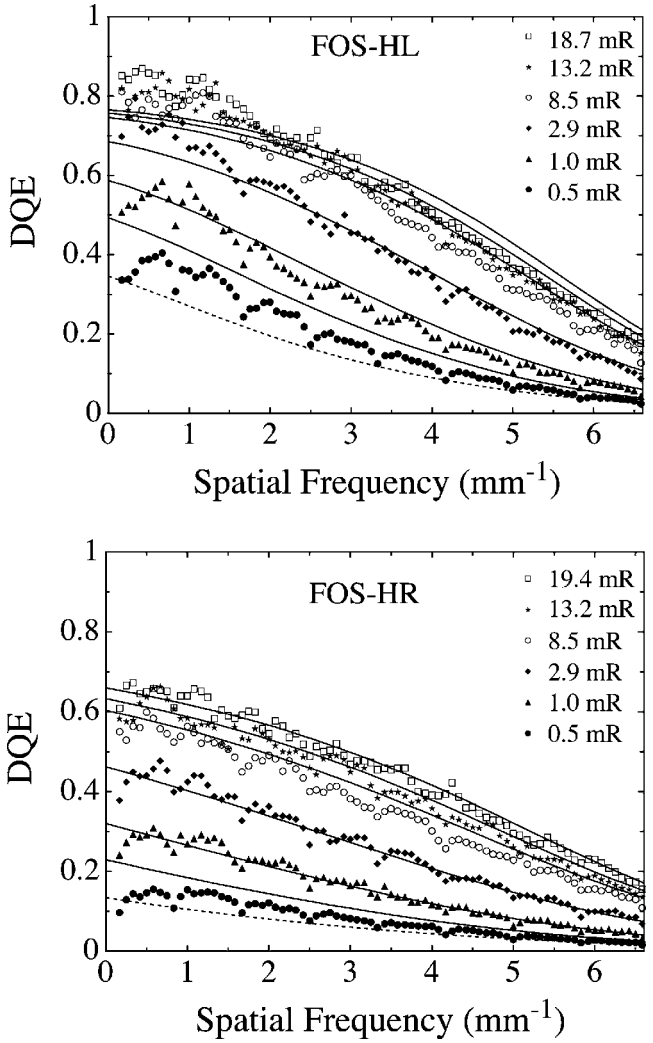

FIG. 8. Detective quantum efficiency (DQE) results associated with (a) the FOS-HL imager configuration and (b) the FOS-HR imager configuration. Measured (symbols) and calculated (solid lines) DQE values, corresponding to the NPS results shown in Fig. 7, are presented for a variety of exposure levels. The dashed lines correspond to DQE values calculated at 0.5 mR for a hypothetical, discrete photodiode array based on a 75 μm pitch array and an optical fill factor of 72%. The assumed value for the optical fill factor (Ref. 22) is based on extrapolation of the aggressive design rules used to make a 127 μm pitch prototype array reported in Ref. 21. Other parameters used in the calculations are the same as those for the HOFFA configurations, with the exception of T_6, which is based on a smaller photodiode aperture due to the lower fill factor.

dance with the shape of the corresponding MTF and the fact that FOS-HL configuration is less influenced by the white noise behavior of the additive dark NPS. The regularly spaced peaks in the NPS observed at low exposures are due to anomalous noise observed in the flood-field images—an effect that is also present in the dark-field images. For both the FOS-HL and FOS-HR configurations, the cascaded system calculations are in reasonable agreement with the measured NPS. There is, however, a discrepancy at high spatial frequencies at the higher exposures (8.5, 13.2, and 19 mR) where the calculations underestimate the measurements. Similar observations can be made for the FOS-HR configuration [Fig. 7(b)], but with a less pronounced effect.

D. Detective quantum efficiency (DQE)

Figures 8(a) and 8(b) show DQE values corresponding to the HOFFA imager configurations employing the FOS-HL and FOS-HR scintillators, respectively. The empirical results, determined from measurements of mean detector signal, MTF and NPS, and incorporating an x-ray fluence of 46 520 x rays/mm^2/mR, are shown for six x-ray exposure levels. For each configuration and exposure level, theoretical calculations based on Eq. (6) are shown and compared to the empirical results.

For the FOS-HL configuration [Fig. 8(a)], DQE results increase with increasing exposure at the lowest exposures (0.5, 1, and 2.9 mR) due to the diminishing contribution of additive noise relative to the total imaging signal. At the highest exposures (8.5, 13.2, and 18.7 mR), the increase in DQE is small and the results start to converge to values that are independent of exposure—indicative of input-quantum-limited operation. Comparison of these empirical results to those obtained from calculations demonstrates reasonably

good agreement. At the highest exposures (8.5, 13.2, and 18.7 mR), the calculations overestimate the measurements at high spatial frequencies.

For the FOS-HR configuration [Fig. 8(b)], DQE results are also seen to increase with increasing exposure due to the diminishing contribution of the additive noise compared to the total imaging signal. In this case, however, the effect is more pronounced due to the lower sensistivity of the FOS-HR scintillator compared to the FOS-HL. For example, at the lowest exposure of 0.5 mR, for which the electronic noise is ~1200 e [rms], the FOS-HL configuration exhibits about a factor of 2 higher DQE at low frequencies compared to the FOS-HR configuration, and a better performance at all frequencies, despite an inferior spatial resolution performance. The advantage of higher spatial resolution offered by the FOS-HR configuration will be reflected in the DQE performance only if the additive noise is reduced or the pixel signal is somehow enhanced, as discussed in the next section. Finally, comparison of the measured DQE results obtained with the FOS-HR to those obtained from the calculations generally demonstrates good agreement.

For purposes of comparison with the results of the HOFFA array, the DQE performance of a hypothetical discrete photodiode array with a 75 μm pitch and an optical fill factor of 72% employing FOS-HL and FOS-HR-type scintillators is shown in Figs. 8(a) and 8(b) (dashed lines), respectively. These calculations, performed at an exposure of 0.5 mR and under assumptions in line with the operation and performance of the HOFFA array, demonstrate the improvement in DQE that can accrue from the incorporation of a continuous photodiode structure.

IV. DISCUSSION AND SUMMARY

The availability of active matrix flat-panel imagers is assisting in the widespread adoption of digital mammography. These imagers provide a variety of advantages common to digital systems, as well as offer the possibility of performing advanced imaging techniques such as tomosynthesis and computed tomography.[13–15] Compared to projection imaging, which is the basis of conventional mammography, such techniques offer advantages that derive from the volumetric information that they provide. Since these techniques require the acquisition of a large number of images per exam, it is highly desirable that the radiation dose per image be kept relatively small so that the total dose does not exceed that employed in conventional mammography. However, significant reduction in the dose per image, which reduces pixel signal size, is problematic for active matrix flat-panel imagers due to the modest gain of these systems compared to a relatively high level of additive noise (on the order of several thousand electrons). As a result, significant reductions in the DQE of both indirect and direct detection active matrix flat-panel mammographic imagers have been reported at low exposures.[6,48,53] Furthermore, the realization of array designs with very high resolution (for example, ~50 μm pitch) faces parallel challenges due to the decreasing signal (due to smaller pixels) and increasing additive noise (due to increased data line capacitance arising from more pixel TFTs along each data line) that are to be anticipated. Therefore, enhancement of the pixel signal relative to additive noise in mammographic flat-panel imager design is highly desirable.

In this paper, the effect of pixel signal enhancement on mammographic imager performance, achieved through maximization of fill factor via replacement of the conventional, discrete, photodiode design with a continuous photodiode structure, has been reported. Studies were performed upon a prototype active matrix flat-panel array (HOFFA) with a 75 μm pixel pitch incorporating such a structure. The array was coupled to two commercially available, structured CsI:Tl scintillators of ~150 μm thickness: one optimized for high light output (FOS-HL) and the other for high spatial resolution (FOS-HR). Pixel signal response results, obtained under mammographic irradiation conditions, indicate that the continuous photodiode design provides a near-unity fill factor. In addition, MTF results from both scintillators demonstrate that the array exhibits good spatial resolution—indicating effective signal isolation between adjacent pixels. At the highest exposures, the DQE is mainly limited by scintillator performance (i.e., by x-ray absorption, sensitivity, Swank factor, and MTF)—representing a desirable outcome. However, at lower exposures, the DQE performance with both scintillators degrades due to the relatively large contribution of additive noise. Under these conditions, the effect of additive noise on DQE was observed to be significantly greater for the FOS-HR scintillator compared to the FOS-HL scintillator, due to the lower sensitivity of the former. It should be noted that the effect of additive noise on DQE would have been reduced had the CsI scintillator been directly deposited on the HOFFA array, thus avoiding a ~40% light loss through the fiber optic substrate. The generally good performance exhibited by the imager demonstrates that a continuous photodiode design can provide a near-unity fill factor that increases the DQE significantly above what would otherwise be possible for an indirect detection flat-panel imager of comparable pitch incorporating discrete photodiodes.

In order to progress from the promise exhibited by the present HOFFA array to clinically practical devices, a variety of improvements are required. For example, elimination of the dark signal drift and reduction of the level of charge trapping exhibited by the HOFFA array down to levels commonly achieved in modern indirect detection arrays with discrete photodiodes (~5%)[34] are necessary and should be achievable. Failure to address these temporal effects will hinder the realization of clinically practical imagers capable of volumetric imaging such as tomosynthesis and CT, where fast image acquisition with minimal temporal artifacts is required.

In addition, arrays incorporating continuous photodiode structures could potentially exhibit increased additive noise due to increased data line capacitance that would increase preamplifier noise [see Eq. (11) below]. For example, the extension of the 75 μm pitch, 3.8×3.8 cm^2 HOFFA design to a full-field array design would result in a data line capacitance of ~96 pF for 24-cm-long lines—about ~50% higher

than what would be expected for a similarly designed array with discrete photodiodes.[22] In addition, extrapolation of such a design to a pixel pitch of 50 μm would further increase the data line capacitance (due to the increased number of pixel TFTs) by an estimated 40%. Encouragingly, beyond the incorporation of the relatively thick, high dielectric constant material (BCB) used to reduce data line capacitance in the present HOFFA array, early studies have demonstrated the possibility of achieving further substantial reduction (of up to a factor of ~5) through additional increases in the BCB thickness, as well as by adopting a lower-capacitance design for the pixel TFTs.[31] Given these considerations, we conservatively estimate that it should be possible to achieve full field, 50 μm pitch continuous photodiode arrays that exhibit data line capacitance on the order of ~100 pF. The minimization of preamplifier noise for such systems will require careful preamplifier circuit design. For the type of preamplifiers commonly used for active matrix flat-panel array readout (including that of the present study), noise performance may be quantified as follows:[54]

$$\sigma_{\mathrm{PREAMP}} = \sigma_0 + \delta C_{\mathrm{input}}, \tag{11}$$

where C_{input} is the input capacitance to the preamplifier circuit (equal to the data line capacitance), and σ_0 and δ are the base noise and noise slope of the preamplifier circuit, respectively—parameters which are determined by the design of the circuit. For example, the preamplifier design used in the present study would provide a preamplifier noise level of ~1500 e [rms] for a C_{input} value of 100 pF. However, a newer design (having a superior base noise and noise slope, but whose packaging precluded its use for the present study) would provide a noise level of ~730 e [rms].[54] (This level of noise assumes operational conditions representative of those required for readout of a full field, 50 μm pitch array at a bandwidth allowing array readout of four frames per second—compatible with the needs of tomosynthesis image capture.) It should be noted that additional reduction in preamplifier noise could be achieved by designing the data lines to run along the 30 cm dimension of a full-field imager and dividing these lines at the center, further lowering the data line capacitance, but requiring preamplifiers and readout at both ends of the array.

Given the aforementioned possibilities and considerations, it is instructive to examine the performance of a hypothetical, full field, 50 μm pitch imager incorporating a continuous photodiode structure. An exposure of 0.5 mR was assumed in the calculations, corresponding to the lower end of the exposure range used for individual projection images performed during a tomosynthesis scan. The calculations are based on the cascaded systems formalism, and the parameters used generally correspond to those employed for the calculations shown in Fig. 8. In addition, the MTF, T_6, is based on a photodiode aperture of 50 μm. Furthermore, an additive noise level of 1500 e [rms] is used—based on calculations using the formalism reported in Ref. 18, and assuming the minimization of data line capacitance and preamplifier noise discussed above as well as a bandwidth allowing a frame rate of 4 fps.

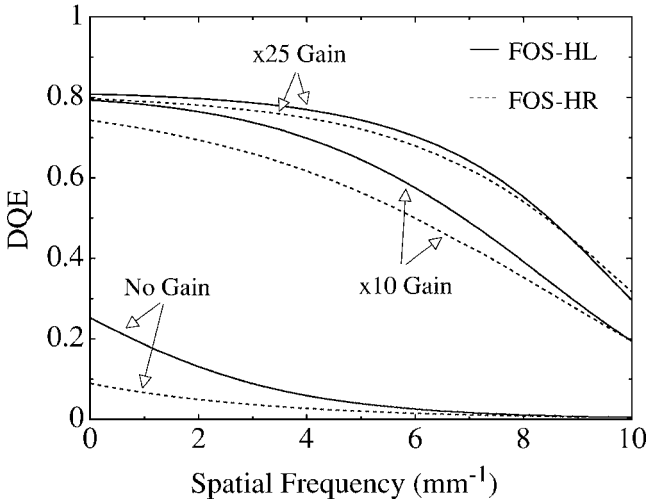

FIG. 9. Calculated DQE results for hypothetical indirect detection imagers based on 50 μm pitch, unity fill factor array designs. Calculations are shown for two imager configurations corresponding to the use of FOS-HL and FOS-HR-type scintillators and were performed at an exposure of 0.5 mR. The calculations labeled "no Gain" correspond to the use of the same parameters and values used in the modeling of the prototype HOFFA imager, with additional assumptions related to the choice of a 50 μm pitch and an additive noise of 1500 e [rms]. For the calculations labeled "×10 Gain" and "×25 Gain," an additional gain stage was introduced following the stage that represents the integration of photons in the photodiode (T_6). For the purposes of the present calculations, this new stage was assumed to be noiseless. See main text for further details.

Figure 9 shows the resulting DQE values for configurations employing FOS-HL and FOS-HR-type scintillators. The combination of small pixels and low exposure leads to modest values of DQE, with the higher sensitivity of the FOS-HL configuration demonstrating better DQE than for the FOS-HR configuration—consistent with the results of Fig. 8. This situation is parallel to that for active matrix flat-panel fluoroscopic imager performance at low exposures, where the relatively modest size of the system gain, relative to the additive noise, strongly constrains the DQE, but can be addressed through enhancements to the gain.[19] It is therefore of interest to examine how significant enhancement of system gain, for example, through the introduction of pixel preamplifiers such as those under development for fluoroscopic imagers,[55,56] would affect mammographic performance in the context of the present discussion. Figure 9 therefore includes two further sets of calculations corresponding to additional gain enhancement of a factor of ×10 and ×25 (corresponding to capabilities that are being developed for fluoroscopy[55]). Such enhancement in gain is observed to dramatically increase DQE, with ×25 enhancement having an incremental, though non-negligible effect compared to ×10 enhancement. These calculations suggest the possibility of achieving high levels of DQE performance from very high resolution active matrix flat-panel mammographic imagers, even at relatively low exposures. The realization of such performance, facilitated by continuous photodiode structures and additional gain-enhancement innovations, could greatly benefit advanced mammographic imaging techniques such as CT and tomosynthesis.

ACKNOWLEDGMENTS

We would like to acknowledge assistance from Douglas Berry with some measurements and data analysis. We also would like to thank Robert Street for valuable discussions concerning the design specifications and operation of HOFFA array, Kyung-Wook Jee for discussions concerning the cascaded systems model, and Mitchell Goodsitt for discussions relating to mammographic imaging. This work was partially supported by National Institute of Health Grant No. 1 RO1 CA-76405.

[a]Electronic mail: elmohri@umich.edu

[1]G. M. Besson, A. Koch, M. Tesic, R. Sottoriva, P. Prieur-Drevron, B. Munier, E. Calais, and P. DeGroot, "Design and evaluation of a slot-scanning full-field digital mammography system," Proc. SPIE **4682**, 457–468 (2002).

[2]M. Lundqvist, M. Danielsson, B. Cederstrom, V. Chmill, A. Chuntonov, and M. Aslund, "Measurements on a full-field digital mammography system with a photon counting crystalline silicon detector," Proc. SPIE **5030**, 547–552 (2003).

[3]S. Thunberg, L. Adelow, O. Blom, A. Coster, J. Egerstrom, M. Eklund, P. Egnell, T. Francke, U. Jordung, T. Kristoffersson, K. Lindman, L. Lindqvist, D. Marchal, H. Olla, E. Penton, V. Peskov, J. Rantanen, S. Solokov, P. Svendenhag, C. Ullberg, and N. Weber, "Dose reduction in mammography with photon counting imaging," Proc. SPIE **5368**, 457–465 (2004).

[4]M. A. Baysal and E. Toker, "A new CMOS-based digital imaging detector for Applications in Mammography," Proc. SPIE **5923**, 1–11 (2005).

[5]L. E. Antonuk, "*a*-Si:H TFT-based active matrix flat-panel imagers for medical x-ray applications," in *Thin Film Transistors, Materials and Processes, Volume 1: Amorphous Silicon Thin Film Transistors*, edited by Y. Kuo (Kluwer, Boston, 2004), pp. 395–484.

[6]S. Vedantham, A. Karellas, S. Suryanarayanan, D. Albagli, S. Han, E. J. Tkaczyk, C. E. Landberg, B. Opsahl-Ong, P. R. Granfors, I. Levis, C. J. D'Orsi, and R. E. Hendrick, "Full breast digital mammography with an amorphous silicon-based flat panel detector: Physical characteristics of a clinical prototype," Med. Phys. **27**, 558–567 (2000).

[7]J. L. Jesneck, R. S. Saunders, E. Samei, J. Q. Xia, and J. Y. Lo, "Detector evaluation of a prototype amorphous selenium-based full field digital mammography system," Proc. SPIE **5745**, 478–485 (2005).

[8]W. Zhao, W. G. Ji, A. Debrie, and J. A. Rowlands, "Imaging performance of amorphous selenium based flat-panel detectors for digital mammography: Characterization of a small area prototype detector," Med. Phys. **30**, 254–263 (2003).

[9]E. D. Pisano and M. J. Yaffe, "Digital mammography," Radiology **234**, 353–362 (2005).

[10]H.-P. Chan, B. Sahiner, M. A. Helvie, N. Petrick, M. A. Roubidoux, T. E. Wilson, D. D. Adler, C. Paramagul, J. S. Newman, and S. Sanjay-Gopal, "Improvement of radiologists' characterization of mammographic masses by using computer-aided diagnosis: A ROC study," Radiology **212**, 817–827 (1999).

[11]J. Jiang, R. Nishikawa, R. A. Schmidt, C. E. Metz, M. L. Giger, and K. Doi, "Improving breast cancer diagnosis with computer-aided diagnosis," Acad. Radiol. **6**, 22–33 (1999).

[12]M. R. Lemacks, S. C. Kappadath, C. C. Shaw, X. Liu, and G. J. Whitman, "A dual-energy subtraction technique for microcalcification imaging in digital mammography: A signal-to-noise analysis," Med. Phys. **29**, 1739–1751 (2002).

[13]L. T. Niklason, B. T. Christian, L. E. Niklason, D. B. Kopans, D. E. Castleberry, B. H. Opsahl-Ong, C. E. Landberg, P. J. Slanetz, A. A. Giardino, R. Moore, D. Albagli, M. C. DeJule, P. F. Fitzgerald, D. F. Fobare, B. W. Giambattista, R. F. Kwasnick, J. Liu, S. J. Lubowski, G. E. Possin, J. F. Richotte, C. Y. Wei, and R. F. Wirth, "Digital tomosynthesis in breast imaging," Radiology **205**, 399–406 (1997).

[14]B. Chen and R. Ning, "Cone-beam volume CT breast imaging: Feasibility study," Med. Phys. **29**, 755–770 (2002).

[15]J. M. Boone, T. R. Nelson, K. K. Lindfors, and J. A. Seibert, "Dedicated breast CT: Radiation dose and image quality evaluation," Radiology **221**, 657–667 (2001).

[16]J. Shaw, D. Albagli, and C.-Y. Wei, "Enhanced *a*-Si/CsI-based flat-panel x-ray detector for mammography," Proc. SPIE **5368**, 370–378 (2004).

[17]K.-W. Jee, L. E. Antonuk, Y. El-Mohri, M. Maolinbay, and Q. Zhao, "Evaluation of direct detection and indirect detection active matrix flat-panel imagers (AMFPIs) for digital mammography," Proc. SPIE **4320**, 13–23 (2001).

[18]M. Maolinbay, Y. El-Mohri, L. E. Antonuk, K.-W. Jee, S. Nassif, X. Rong, and Q. Zhao, "Additive noise properties of active matrix flat-panel imagers," Med. Phys. **27**, 1841–1854 (2000).

[19]L. E. Antonuk, K.-W. Jee, Y. El-Mohri, M. Maolinbay, S. Nassif, X. Rong, Q. Zhao, J. H. Siewerdsen, R. A. Street, and K. S. Shah, "Strategies to improve the signal and noise performance of active matrix, flat-panel imagers for diagnostic x-ray applications," Med. Phys. **27**, 289–306 (2000).

[20]S. Muller, "Full-field digital mammography designed as a complete system," Eur. J. Radiol. **31**, 25–34 (1999).

[21]R. L. Weisfield, W. Yao, T. Speaker, K. Zhou, R. E. Colbeth, and C. Proano, "Performance analysis of a 127-micron pixel large-area TFT/photodiode array with boosted fill factor," Proc. SPIE **5368**, 338–348 (2004).

[22]W. Yao, dpiX (private communication, 2006).

[23]J. T. Rahn, F. Lemmi, R. L. Weisfield, R. Lujan, P. Mei, J. P. Lu, J. Ho, S. Ready, R. B. Apte, P. Nylen, J. B. Boyce, and R. A. Street, "High-resolution high fill factor *a*-Si:H sensor arrays for medical imaging," Proc. SPIE **3659**, 510–517 (1999).

[24]M. Mulato, F. Lemmi, R. Lau, J. P. Lu, J. Ho, S. E. Ready, J. T. Rahn, and R. A. Street, "Charge collection and capacitance in continuous film flat-panel detectors," Proc. SPIE **3977**, 26–37 (2000).

[25]I. A. Cunningham, M. S. Westmore, and A. Fenster, "A spatial-frequency dependent quantum accounting diagram and detective quantum efficiency model of signal and noise propagation in cascaded imaging systems," Med. Phys. **21**, 417–427 (1994).

[26]J. H. Siewerdsen, L. E. Antonuk, Y. El-Mohri, J. Yorkston, W. Huang, and I. A. Cunningham, "Signal, noise power spectrum, and detective quantum efficiency of indirect-detection flat-panel imagers for diagnostic radiology," Med. Phys. **25**, 614–628 (1998).

[27]M. Mulato, S. Ready, K. Van Schuylenbergh, J. P. Lu, and R. A. Street, "Crosstalk and lateral conduction effects in continuous-sensor amorphous silicon imagers," J. Appl. Phys. **89**, 8193–8201 (2001).

[28]G. Pang, W. Zhao, and J. A. Rowlands, "Digital radiology using active matrix readout of amorphous selenium: Geometrical and effective fill factors," Med. Phys. **25**, 1636–1646 (1998).

[29]J. T. Rahn, F. Lemmi, J. P. Lu, P. Mei, R. A. Street, S. Ready, J. Ho, R. B. Apte, K. Van Schuylenbergh, R. Lau, R. L. Weisfield, R. Lujan, and J. Boyce, "Achieving high-resolution in flat-panel imagers for digital radiography," Proc. SPIE **3770**, 136–145 (1999).

[30]F. Lemmi, J. T. Rahn, and R. A. Street, "Lateral conduction in structured amorphous silicon $p(+)$-i-$n(+)$ photodiodes," J. Non-Cryst. Solids **266**, 1203–1207 (2000).

[31]M. Mulato, J. P. Lu, and R. A. Street, "Simulated and measured data-line parasitic capacitance of amorphous silicon large-area image sensor arrays," J. Appl. Phys. **89**, 638–647 (2001).

[32]R. A. Street, "Thermal generation currents in hydrogenated amorphous-silicon p-i-n structures," Appl. Phys. Lett. **57**, 1334–1336 (1990).

[33]L. E. Antonuk, J. Boudry, W. Huang, D. L. McShan, E. J. Morton, J. Yorkston, M. J. Longo, and R. A. Street, "Demonstration of megavoltage and diagnostic x-ray imaging with hydrogenated amorphous silicon arrays," Med. Phys. **19**, 1455–1466 (1992).

[34]L. E. Antonuk, Y. El-Mohri, J. H. Siewerdsen, J. Yorkston, W. Huang, V. E. Scarpine, and R. A. Street, "Empirical investigation of the signal performance of a high-resolution, indirect detection, active matrix flat-panel imager (AMFPI) for fluoroscopic and radiographic operation, Med. Phys. **24**, 51–70 (1997).

[35]T. Document, "FOS (fiber optic plate scintillator) for digital x-ray imaging," Hamamatsu Photonics K. K. 1998.

[36]W. Huang, L. E. Antonuk, J. Berry, M. Maolinbay, C. Martelli, P. Mody, S. Nassif, and M. Yeakey, "An asynchronous, pipelined, electronic acquisition system for active matrix flat-panel imagers (AMFPIs)," Nucl. Instrum. Methods Phys. Res. A **431**, 273–284 (1999).

[37]R. J. Yarema, T. Zimmerman, J. Srage, L. E. Antonuk, J. Berry, W. Huang, and M. Maolinbay, "A programmable, low noise, multichannel ASIC for readout of pixelated amorphous silicon arrays," Nucl. Instrum. Methods Phys. Res. A **439**, 413–417 (2000).

[38]*ACR Mammography Quality Control Manual*, American College of Radiology, 1999.
[39]H. Fujita, D. Tsai, T. Itoh, K. Doi, J. Morishita, K. Ueda, and A. Ohtsuka, "A simple method for determining the modulation transfer function in digital radiography," IEEE Trans. Med. Imaging **11**, 34–39 (1992).
[40]Y. El-Mohri, L. E. Antonuk, Q. Zhao, M. Maolinbay, X. Rong, K. W. Jee, S. Nassif, and C. Cionca, "A quantitative investigation of additive noise reduction for active matrix flat-panel imagers using compensation lines," Med. Phys. **27**, 1855–1864 (2000).
[41]Y. El-Mohri, K. W. Jee, L. E. Antonuk, M. Maolinbay, and Q. Zhao, "Determination of the detective quantum efficiency of a prototype, megavoltage indirect detection, active matrix flat-panel imager," Med. Phys. **28**, 2538–2550 (2001).
[42]J. C. Dainty and R. Shaw, *Image Science: Principles, Analysis and Evaluation of Photographic Type Imaging Processes* (Academic, London, 1974).
[43]M. L. Giger, K. Doi, and C. E. Metz, "Investigation of basic imaging properties in digital radiography. 2. Noise Wiener spectrum," Med. Phys. **11**, 797–805 (1984).
[44]A. D. Maidment and M. J. Yaffe, "Analysis of the spatial-frequency-dependent DQE of optically coupled digital mammography detectors," Med. Phys. **21**, 721–729 (1994).
[45]J. T. Dobbins, III, D. L. Ergun, L. Rutz, D. A. Hinshaw, H. Blume, and D. C. Clark, "DQE(f) of four generations of computed radiography acquisition devices," Med. Phys. **22**, 1581–1593 (1995).
[46]I. A. Cunningham and R. Shaw, "Signal-to-noise optimization of medical imaging systems," J. Opt. Soc. Am. A Opt. Image Sci. Vis **16**, 621–632 (1999).
[47]M. Rabbani, R. Shaw, and R. Vanmetter, "Detective quantum efficiency of imaging systems with amplifying and scattering mechanisms," J. Opt. Soc. Am. A Opt. Image Sci. Vis **4**, 895–901 (1987).
[48]K.-W. Jee, L. E. Antonuk, Y. El-Mohri, and Q. Zhao, "System performance of a prototype flat-panel imager operated under mammographic conditions," Med. Phys. **30**, 1874–1890 (2003).
[49]J. M. Boone, T. R. Fewell, and R. J. Jennings, "Molybdenum, rhodium, and tungsten anode spectral models using interpolating polynomials with application to mammography," Med. Phys. **24**, 1863–1874 (1997).
[50]J. M. Boone, "Spectral modeling and compilation of quantum fluence in radiography and mammography," Proc. SPIE **3336**, 592–601 (1998).
[51]R. J. Pizzutiello and J. E. Cullinan, *Introduction to Medical Radiographic Imaging* (Eastman Kodak Company, Rochester, NY, 1993).
[52]R. A. Street, S. Ready, L. Melekhov, J. Ho, A. Zuck, and B. Breen, "Approaching the theoretical x-ray sensitivity with HgI2 direct detection image sensors," Proc. SPIE **4682**, 414–422 (2002).
[53]W. Zhao, R. Deych, and E. Dolazza, "Optimization of operational conditions for direct digital mammography detectors for digital tomosynthesis," Proc. SPIE **5745**, 1272–1281 (2005).
[54]M. Maolinbay, T. Zimmerman, R. J. Yarema, L. E. Antonuk, Y. El-Mohri, and M. Yeakey, "Design and performance of a low noise, 128-channel ASIC preamplifier for readout of active matrix flat-panel imaging arrays," Nucl. Instrum. Methods Phys. Res. A **485**, 661–675 (2002).
[55]L. E. Antonuk, Y. Li, H. Du, Y. El-Mohri, Q. Zhao, J. Yamamoto, A. R. Sawant, Y. Wang, Z. Su, J. P. Lu, R. A. Street, R. L. Weisfield, and B. Yao, "Investigation of strategies to achieve optimal DQE performance from indirect detection, active matrix, flat-panel imagers (AMFPIs) through novel pixel amplification architectures," Proc. SPIE **5745**, 18–31 (2005).
[56]Y. Li, L. E. Antonuk, Y. El-Mohri, Q. Zhao, H. Du, A. Sawant, and Y. Wang, "Effect of x-ray irradiation on polycrystalline silicon thin-film transistors," J. Appl. Phys. **99**, 64501 (1–7) (2006).
[57]L. E. Antonuk, Y. El-Mohri, A. Hall, K.-W. Jee, M. Maolinbay, S. C. Nassif, X. Rong, J. H. Siewerdsen, Q. Zhao, and R. L. Weisfield, "A large-area, 97 μm pitch, indirect-detection, active matrix, flat-panel imager (AMFPI)," Proc. SPIE **3336**, 2–13 (1998).
[58]N. Jung, P. L. Alvie, F. Busse, N. Conrads, H. M. Meulenbrugge, W. Rutten, U. Schiebel, M. Meibrecht, and H. Wieczorek, "Dynamic x-ray imaging system based on an amorphous silicon thin-film array," Proc. SPIE **3336**, 510–517 (1998).